The Ventilation Effect on Stator Convective Heat Transfer of an Axial-Flux Permanent-Magnet Machine

Yew Chuan Chong, Estanislao J. P. Echenique Subiabre, Markus A. Mueller, *Member, IEEE*, John Chick, David A. Staton, and Alasdair S. McDonald

***Abstract*—This paper investigates the effect of the inlet configuration on cooling for an air-cooled axial-flux permanent-magnet (AFPM) machine. Temperature rises in the stator were measured and compared with results predicted using computational fluid dynamic (CFD) methods linked to a detailed machine loss characterization. It is found that an improved inlet design can significantly reduce the stator temperature rises. Comparison between the validated CFD model results and the values obtained from heat transfer correlations addresses the suitability of those correlations proposed specifically for AFPM machines.**

***Index Terms*—Air cored, cooling, direct drive, eddy currents, electric machines, fluid dynamics, loss measurement, permanent-magnet machines, thermal analysis.**

NOMENCLATURE

Mechanical symbols

A	Cross-sectional area of a flow path (in square meters).
Δ	Finite difference.
c_p	Specific heat (in joules per kilogram kelvin).
e	Internal energy per unit mass (in joules per kilogram).
E	Energy (in joules).
ε	Turbulent dissipation rate (in square meters per cubic second).
g	Gravitational acceleration (in meters per square second).
G	Gap ratio, s/R (dimensionless).
$\overline{h}$	Mean convection heat transfer coefficient (in watts per square meter kelvin).
K	Turbulent kinetic energy (in square meters per square second).
k_{air}, k_t, k_i, k_j, k_{sol}	Thermal conductivities of air, turbulence, insulation, impregnation materials, and solid components (in watts per meter kelvin).
K	Pressure loss coefficient (dimensionless).
l_i, l_j	Material thicknesses (in meters).
$\dot{m}$	Mass flow rate (in kilograms per second).
μ, μ_t	Dynamic viscosity and turbulent viscosity (in pascal seconds).
$\overline{\mathrm{Nu}}$	Mean Nusselt number (dimensionless).
ω	Specific dissipation rate (in per second).
ω_m	Angular velocity (in radians per second).
p, p_{in}, p_{tot}	Static, rotor pumping, and total gauge pressures (in pascals).
Pr_t	Turbulent Prandtl number (dimensionless).
q''	Heat flux (in watts per square meter).
Q	Volumetric flow rate (in cubic meters per second).
r, R	Radius and rotor outer radius (in meters).
ρ	Density (in kilograms per cubic meter).
R_{th}	Thermal contact resistance (in square meter kelvins per watt).
Re_θ	Rotational Reynolds number (dimensionless).
s	Axial gap distance (in meters).
S_T	Heat generation per unit volume (in watts per cubic meter).
S_{ij}	Strain rate tensor (in per second).
T, T_w, T_{ref},	Temperature, wall temperature, and reference temperature (in degrees Celsius or kelvins).
τ_w	Wall shear stress (in pascals).
u, V	Velocities (in meters per second).
u^+	Friction velocity (dimensionless).
W_{in}, W_{out}	Work transfer to and from a system (in joules).
y	Normal distance from the wall (in meters).
y^+	Dimensionless wall distance.
z	Elevation above a reference plane (in meters).

Electrical symbols

α_{Cu}, α_{core}	Copper and core thermal resistivity coefficients (in per kelvin).

Manuscript received February 27, 2013; revised May 31, 2013; accepted July 27, 2013. Date of publication October 1, 2013; date of current version February 7, 2014. This work was supported in part by Motor Design Ltd., NGenTec Ltd., The University of Edinburgh, and the Energy Technology Partnership.

Y. C. Chong, E. J. P. Echenique Subiabre, M. A. Mueller, and J. Chick are with the Institute for Energy Systems, The University of Edinburgh, Edinburgh EH9 3JL, U.K. (e-mail: y.chong@ed.ac.uk; E.Echenique-Subiabre@ed.ac.uk; markus.mueller@ed.ac.uk; john.chick@ed.ac.uk).

D. A. Staton is with Motor Design Ltd., Ellesmere SY12 0EG, U.K. (e-mail: dave.staton@motor-design.com).

A. S. McDonald is with the Department of Electronic and Electrical Engineering, University of Strathclyde, Glasgow G1 1XW, U.K. (e-mail: alasdair.mcdonald@strath.ac.uk).

Color versions of one or more of the figures in this paper are available online at http://ieeexplore.ieee.org.

Digital Object Identifier 10.1109/TIE.2013.2284151

B_g	Peak value of air-gap flux density due to the permanent magnets.
$\hat{B}_{0\mathrm{Fe}}$, $\hat{B}_{0\mathrm{PM}}$	Amplitudes of flux reaction in the iron and magnets.
d_w	Wire diameter.
σ_{PM}, σ_{Fe}	Magnetic skin depths (PM for magnets and Fe for iron).
ΔT_{coil}	Temperature rise in coils above ambient temperature (in degrees Celsius or kelvins).
EMF	Back-electromotive-field open-circuit phase voltage.
f	Electric frequency (in hertz).
h_{PM}	Magnet height.
I_{rms}	Phase rms current (in amperes).
k_{circ}, k_{eddy}	Constants for circulating and eddy current losses (in $\mathrm{N \cdot m \cdot (rad/s)^{-1}}$).
k_m	Constant for mechanical losses (in newton meters).
μ_0	Permeability of free space (in henrys per meter).
μ_r, μ_{PM}, μ_{Fe}	Relative magnetic permeabilities (PM for magnets and Fe for iron).
N_t	Number of turns per coil.
v	Speed of the flux reaction wave.
P_{mech}	Mechanical input power (in watts).
P_{Cu}, P_{rotor}	Copper losses in the coils and rotor.
P_{load}	Output power dissipated into the resistive load (in watts).
P_w	Loss due to eddy and circulating currents in the coils (in watts).
$P_{\mathrm{eddy\text{-}coils}}$	Eddy current loss in coils (in watts).
$P_{\mathrm{mech\text{-}loss}}$	Mechanical loss (in watts).
$P_{\mathrm{no\text{-}load}}$	No-load loss (in watts).
$P_{\mathrm{eddy}_{\mathrm{PM}}}$, $P_{\mathrm{eddy}_{\mathrm{Fe}}}$	Eddy current losses in the magnets and iron (in watts).
$R_{\mathrm{Cu}}^{\mathrm{amb}}$	Copper phase resistance at ambient temperature (in ohms).
R_{rotor}	Equivalent rotor resistance (in ohms).
R_{eddy}	Equivalent resistance to represent eddy current loss in coils (in ohms).
R_{eq}	Thevenin resistance of the generator seen by the load (in ohms).
R_{circ}	Equivalent winding resistance to represent circulating current loss.
R_{load}	Load resistance (in ohms).
ρ_{Cu}, ρ_{Fe}, ρ_{PM}	Copper, iron, and magnet resistivities.
ω_s	Electric angular frequency (in radians per second).
L_s	Synchronous phase inductance (in henrys).
L_m	Mean turn length covered by the magnet (in meters).

I. Introduction

DUE TO the development in high-performance rare-earth permanent-magnet technology, axial-flux permanent-magnet (AFPM) machines are an attractive solution for many applications such as hybrid and electric vehicles [1], as well as wind turbine generators [2]. Owing to the high remanent magnetic field, the use of neodymium magnets (NdFeB) can meet industry demands such as high power density, efficiency, and cost reduction. This has opened up great opportunities for novel machine topologies to be developed [3], [4]. AFPM machines have noticeably short axial length because the disk-shaped stator and rotor are placed face to face coaxially. However, if proper cooling is not considered in the design process, the compact construction of AFPM machines can result in a high temperature rise. Existing cooling design techniques have been developed mostly for conventional radial-flux machines and at a time when power density was not so much of an issue. More effort should be given to thermal analysis to fully exploit new topologies [5] and materials [6]. Indeed, overheating can cause detrimental effects to machine lifetime, reliability, electrical efficiency, demagnetization of magnets, and insulation failure. The latest approaches for thermal analysis of electrical machines have been reviewed in [7]–[9].

Effective ventilation can be a very economical cooling method for electrical machines because of the high temperature difference between the cooling air and heated surface. For a self-cooled AFPM machine, the air adjacent to the rotor is dragged by the rotor due to the no-slip condition and driven radially outward by the centrifugal force [10]. Hence, the rotor movement creates a pressure difference to draw the air from the surroundings toward the rotor center to replace the cooling air which has been pumped out. Moreover, the protruding magnets on the rotor assist the pumping effect. Heat generated in the machine is transferred to the radial outflow by forced convection. However, due to the topologies of AFPM machines, this flow phenomenon is subjected to a degree of restriction.

Two main flow regimes are exhibited in a flat rotating disk facing a stationary disk: Batchelor flow [11] and Stewartson flow [12]. The Batchelor flow normally describes the flow structure with the radial outflow adjacent to the rotor, replaced by the radial inward flow adjacent to the stator from the periphery to satisfy the conservation of mass. The distinction between Batchelor flow and Stewartson flow is that Batchelor flow has an inviscid rotating fluid core between separate tangential boundary layers of the rotating and stationary disks, respectively, and at almost zero radial velocity. Batchelor flow is more likely to occur in enclosed systems, whereas Stewartson flow tends to appear in open and throughflow-ventilated systems. Convective heat transfer has been investigated for open rotor–stator systems in [13]–[16] and enclosed rotor-stator systems in [17]. The convective heat transfer correlations that have been developed for these systems show that the Nusselt number mainly depends on the rotational Reynolds number $\mathrm{Re}_\theta = \rho\omega_m R^2/\mu$ and the gap ratio $G = s/R$.

In [18], the authors studied the cooling performance of an AFPM machine by blocking the ventilation holes at the rotor inner radius. It was demonstrated that the measured temperatures were higher than the cases with ventilation holes unblocked. Throughflow-ventilated AFPM machines are usually designed with a degree of ventilation to allow the surrounding air passing through. However, the literature that describes the effect of inlet configuration of an AFPM machine on cooling in detail is limited. A rotor hub with radial blades to assist in

pumping air through an AFPM machine was proposed in [19]. In fact, both Batchelor and Stewartson flows can coexist in the rotor-stator gap of throughflow-ventilated AFPM machines. At the outer radius, there will be both inflow and outflow of air; at the inner radius, there will be just radial outflow [16]. This occurs as the supply of air to the rotor-stator gap provided from the flow entry at or near the rotating axis does not match the net radial outflow exiting from the rotor-stator gap. The mode of flow in the rotor-stator gap is mainly dependent on the machine speed and ventilation design.

For surface-mounted permanent-magnet machines (i.e., rotor with protrusions), linear correlations based only on the rotational Reynolds number and the gap ratio for mean Nusselt number were proposed in [16]. They were based upon the experimental measurements for stator convective heat transfer using a mock-up throughflow-ventilated rotor-stator system. In [20], the effects of variation of rotor-stator gap spacing, magnet depth, and rotational speed to convective heat transfer were investigated through computational fluid dynamic (CFD) modeling with experimental verification on mass flow rate and temperatures. Also, a complex correlation was proposed to predict their influences on stator convective heat transfer variation with radial position. In [21], using simplified free rotating disk correlations for AFPM machines, the lumped-parameter thermal network developed shows reasonable temperature estimation. However, in surface-mounted permanent-magnet machines, correlations like the ones proposed in [20] can give better agreement.

Since the stator is commonly sandwiched between two rotor disks in AFPM machine topologies, the subject of this paper is to investigate the effect of inlet configuration at the rotor on convective heat transfer between air and the stator, facing two moving rotors with protruding magnets at a distance s from the stator, with no air flow imposed on the system. This study provides an important insight to machine designers of how convective cooling can be enhanced for AFPM machines with improved ventilation design. Since the electromagnetic and thermal aspects are linked, a detailed power loss distribution in the machine is presented in Section IV. The electrical losses provide the heat sources and inputs to the CFD models described in Section V. Additionally, the simulation of heat transfer is coupled with air flow modeling for conjugate heat transfer analysis. The measured temperatures in a 25-kW AFPM prototype validate the CFD models.

II. Background

A. Conservation of Mass and Energy

Fig. 1 shows a control volume representing the AFPM machine. The ambient air passes through at a steady rate of mass flow $\dot{m}$, entering at position 1 and leaving at position 2. The air is incompressible in the present study. Based on the principle of conservation of energy, the fluid flow through a control volume can be analyzed using the steady flow energy equation (SFEE) [22]

$$W_{\text{in}} - W_{\text{out}} = \Delta E_{1-2}. \tag{1}$$

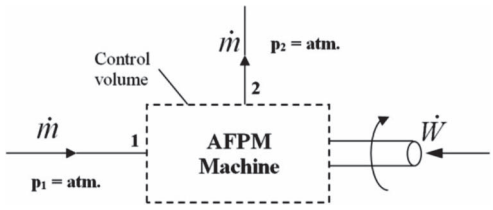

Fig. 1. Control volume showing sign convention for work transfer.

ΔE_{1-2} is the change of energy from state 1 to state 2; W_{in} and W_{out} are the energies supplied to and leaving from the system, respectively. Since the air flow through the control volume is only the focus, heat transfer is not considered in this section, but it is included in Section V. Equation (1) can be expanded and expressed in terms of pressure as

$$p_{\text{in}} - (p_2 - p_1) = \rho(e_2 - e_1) + \frac{\rho(V_2^2 - V_1^2)}{2} + \rho g(z_2 - z_1). \tag{2}$$

The rotor with surface-mounted permanent magnets is a fanlike device. As the rotor is rotated at a given speed, p_{in} is the rotor pumping pressure that drives the air through the control volume. V_i (where $i = \{1, 2\}$) is the air velocity, z_i is the elevation above datum, e_i is the internal energy per unit mass, and p_i is the static pressure.

B. Relationship Between Rotor Characteristics and System Flow Resistance

Apparently, it is shown that (2) is in the form of Bernoulli equation by the shear forces being present. The pressure term p can be ignored as both inlet and outlet boundaries are atmospheric. By assuming that the boundaries of the control volume are located sufficiently far from the entry and periphery of the AFPM machine, thus V_1 and V_2 are equal; the kinetic energy terms $\rho V^2/2$ can be then cancelled out. Since the working fluid is air, the potential energy term $\rho g z$ is negligible. Hence, the SFEE can be reduced to

$$p_{\text{in}} = \rho \Delta e. \tag{3}$$

The term $\rho \Delta e$ represents the system pressure loss and is usually defined in the form of $K \rho u^2/2$ as

$$p_{\text{in}} = \frac{\rho Q^2}{2} \times \sum_{i=1}^{n} \left(\frac{K_i}{A_i^2} \right). \tag{4}$$

K is the pressure loss coefficient, and A_i is the local cross-sectional area of the flow path in the AFPM machine. According to (4), the air flow rate through the machine is not only dependent on the rotor pumping pressure but also affected by the system flow resistance. The pressure losses in the AFPM machine are caused by friction loss, inlet loss, shock loss, leakage loss, and other losses due to flow separation from the walls. Determination of the degree of these losses of a fanlike device is difficult to calculate analytically and is outside the scope of this paper. However, by reducing these pressure losses, an increase in mass flow rate is obtainable for a given speed. In this paper, the inlet loss is investigated to study the impact of inlet configuration to machine cooling.

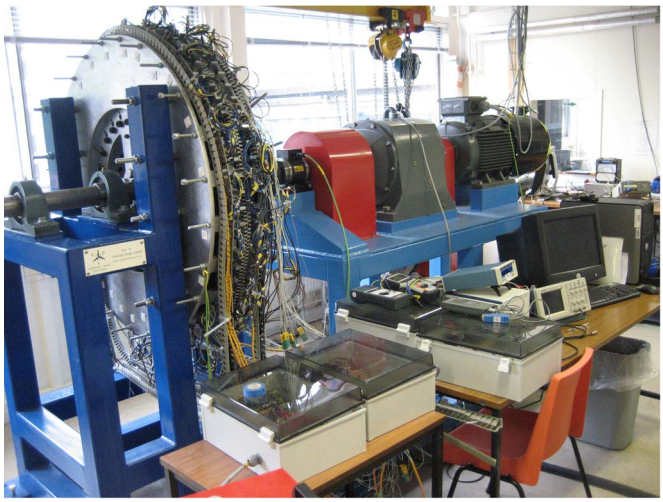

Fig. 2. Twenty-five-kilowatt AFPM prototype at the experimental test facility.

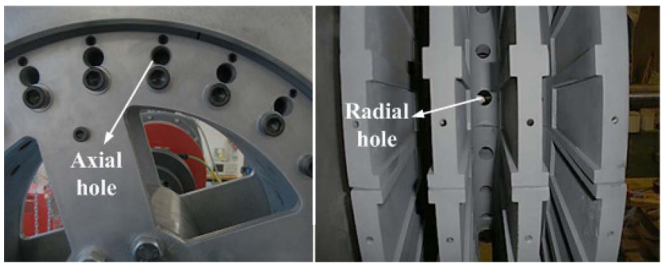

Fig. 3. Ventilation holes.

III. Experimental Test Facility

A. AFPM Machine

Fig. 2 shows a 25-kW 100-r/min generator driven by means of an inverter-fed induction machine through a step-down gearbox. This is an air-cooled AFPM prototype with three axial stages developed by NGenTec Ltd. for direct-drive application [23]. The inner and outer radii of the rotor are 220 and 460 mm, respectively. The running clearance between the rotor and stator is 3.5 mm, providing a gap ratio of 0.0076.

B. Machine Ventilation

The prototype is ventilated by 24 radial and axial holes, respectively, on the rotor at the inner radius, as illustrated in Fig. 3. The outer edge of the AFPM machine is unshrouded. Both axial and radial holes have the same diameter of 20 mm, and the axial holes are located at a radius of 272 mm. Different arrangements of the air inlet holes can be tested by blocking the unnecessary holes using a tape. Three cases were considered:

1) all holes unblocked;
2) only radial holes unblocked;
3) only axial holes unblocked.

C. Temperature Measurement

Since copper loss is the major loss component in this machine topology, the temperature rises of stator coils were recorded during the tests. Thermocouples were embedded in the stator to measure the local temperatures at the coils. Thermocouples A, B, and C measure the coil surface temperatures at the outer radius, midradius, and inner radius, respectively, as shown in Fig. 4, and the experimental heating curves are illustrated in Fig. 5. Since the generator is stator critical, temperature measurement was not performed on the rotor. In addition, the electrical resistance of the coils after steady state was also measured.

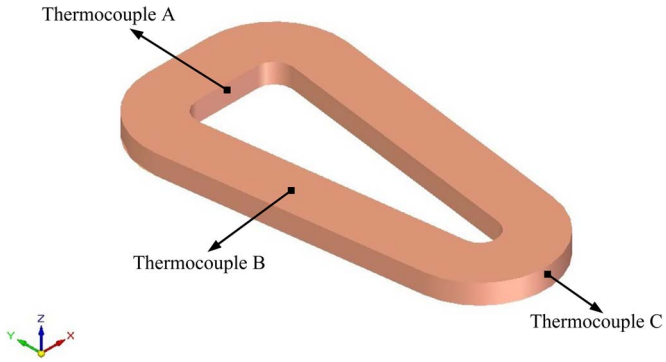

Fig. 4. Locations of the thermocouples on the stator coil.

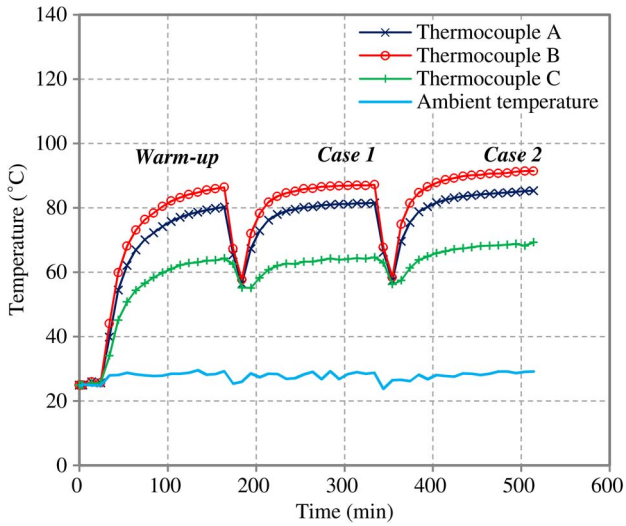

Fig. 5. Heating curves of warm-up, Case 1, and Case 2.

Only one stage (nondrive end) of the generator was loaded with a three-phase resistive load during the tests, because this stage was assembled with the same stator modules. Since this prototype was also assembled with different stator module designs, loading the drive end and middle stages may affect the consistency of temperature measurement. The machine was warmed up at full load before the ventilation tests were carried out until steady state was achieved. There was an interval of 20 min of cooling (disconnecting the load) after warm-up and testing, so that the ventilation tests were conducted under the same operating conditions.

IV. Power Loss Calculation

This section describes the procedure of evaluating the power losses of the prototype. The main loss occurs in the windings

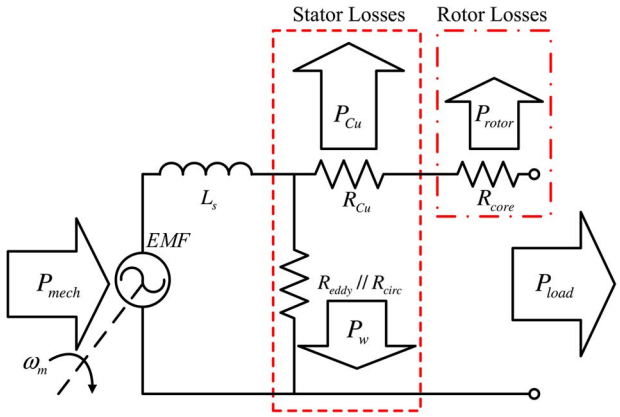

Fig. 6. Circuital representation of electrical losses in an air-cored machine.

(approximately 84% of electrical losses), although a complete analysis of the remaining losses is provided.

Losses in the electrical machine are in mechanical and electrical forms. Since direct-drive topologies rotate at low speed, the mechanical losses (bearing and windage losses) have a negligible contribution to the machine power losses. Moreover, due to the use of an air-cored stator, the cogging torque is zero. Hence, the electrical losses can be considered as the main losses, and they are fed into the CFD model as the inputs of heat sources.

A. Electrical Losses in an Air-Cored Machine

In the stator, which is ironless, all losses are therefore in the copper coils. Both no-load and load losses need to be considered. No-load losses are caused by the action of the rotating field of the magnets inducing eddy and circulating currents in the coils. Circulating currents exist in parallel-connected coils because of the induced voltage differences between the coils. They behave like additional Joule heating in the windings even when the machine is running at no load. Finally, the phase currents produce I^2R loss in the winding.

In the rotor (magnets and core back iron), a smaller portion of losses occur compared to the stator, and they occur only when the machine is loaded. At rated speed, the rotor losses account for only 16% of the total electrical losses. The reaction field from the windings (armature reaction) creates asynchronous time-varying fluxes on the rotor, causing eddy current losses in the magnets and the iron supporting them. As hysteresis losses are negligible at low electrical frequencies [24], their calculation is omitted in this paper. A summary of electrical losses is depicted in Fig. 6.

B. Method for Electrical Losses

1) Theoretical Background: Eddy currents in the windings can be estimated using the well-known Carter formula [26] which is accurate at low electrical frequencies (i.e., $f \leq 50$ Hz) [27]

$$P_{\mathrm{eddy}_{\mathrm{coils}}} = \frac{(\pi^3 B_g^2 d^4 f^2 L_m N_t)}{4\rho_{\mathrm{Cu}}(1+\alpha_{\mathrm{Cu}}\Delta T_{\mathrm{coil}})}. \tag{5}$$

Copper and rotor losses are calculated using

$$P_{\mathrm{Cu}} = 3I_{\mathrm{rms}}^2 R_{\mathrm{Cu}}^{\mathrm{amb}}(1+\alpha_{\mathrm{Cu}}\Delta T_{\mathrm{coil}}) \tag{6}$$

$$P_{\mathrm{rotor}} = \left(3I_{\mathrm{rms}}^2 R_{\mathrm{core}}\right)/(1+\alpha_{\mathrm{core}}\Delta T_{\mathrm{core}}). \tag{7}$$

The core resistance R_{core} in Fig. 6 lumps together the magnet and iron losses. Since the thermal resistivity coefficients of the iron and neodymium magnets are approximately 300 and 4000 times lower than the copper, respectively (for the thermal operating range of 0–120 °C), it is plausible to neglect the changes of resistivity in the magnets and iron and simply estimate rotor losses as $P_{\mathrm{rotor}} \approx 3I_{\mathrm{rms}}^2 R_{\mathrm{core}}$.

Additionally, the phase current I_{rms} for a machine connected to a resistive load (R_{load}) is obtained from

$$\mathrm{EMF}^2 = (V_{\mathrm{load}} + R_{\mathrm{eq}} I_{\mathrm{rms}})^2 + (\omega_s L_s I_{\mathrm{rms}})^2 \tag{8}$$

$$I_{\mathrm{rms}} = \frac{\mathrm{EMF}}{\sqrt{R_{\mathrm{load}}^2 + 2R_{\mathrm{load}}R_{\mathrm{eq}} + R_{\mathrm{eq}}^2 + (\omega_s L_s)^2}}. \tag{9}$$

As $R_{\mathrm{eddy}}//R_{\mathrm{circ}} \gg \omega_e L_s$ from Fig. 6, the equivalent Thevenin resistance R_{eq} of the generator considering the thermal effect in the copper only is given by

$$R_{\mathrm{eq}} = R_{\mathrm{Cu}}^{\mathrm{amb}}(1+\alpha_{\mathrm{Cu}}\Delta T_{\mathrm{coil}}) + R_{\mathrm{core}}. \tag{10}$$

Copper resistance can be easily estimated. However, the core resistance requires a more complex approach which is out of the scope of this paper. An alternative calculation can be done using finite-element analysis or by the locked-rotor test as explained in Section IV-B3.

2) Experimental Calculations of Eddy and Circulating Current Losses in the Windings: Eddy and circulating current losses were determined by the no-load tests from standstill to rated speed. Torque input and mechanical speed were measured at the shaft of the generator in steady-state conditions. At low speed, the mechanical losses are linearly proportional to the rotational speed, whereas eddy and circulating current losses are directly proportional to the square of rotational speed. Mechanical and electrical losses are modeled in (11) and (12). The constants k_m and k_{eddy} are obtained by fitting the experimental data (summarized in Fig. 7) to a second-order polynomial. The circulating current coefficient k_{circ} is obtained from the segregation of losses

$$P_{\mathrm{mech\text{-}loss}} = k_m \omega_m \tag{11}$$

$$P_w = (k_{\mathrm{eddy}} + k_{\mathrm{circ}})\omega_m^2 \tag{12}$$

$$P_{\mathrm{no\text{-}load}} = P_w + P_{\mathrm{mech\text{-}loss}}. \tag{13}$$

Segregation between eddy and circulating current losses is possible by performing the no-load test twice: with disconnected coils and parallel connection. Unfortunately, the mechanical losses increase when the circulating current is flowing into the windings due to the effects of an unwanted ripple in the torque. Nevertheless, the authors assumed that, at low speed, the mechanical losses have no impact on the heat generation. Table I summarizes the experimental constants for the no-load losses. The eddy and circulating current losses at 100 r/min are

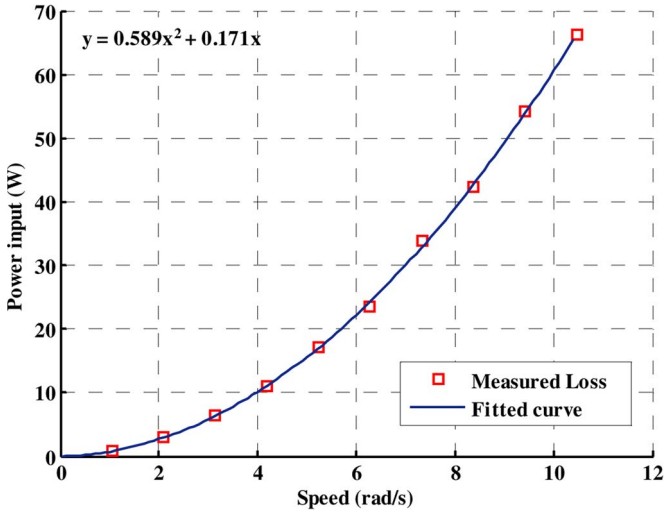

Fig. 7. No-load losses (disconnected coils) fitted to a second-order polynomial. The first coefficient (0.589) represents k_{eddy}, and the second one (0.171) represents k_m.

TABLE I
MECHANICAL, EDDY, AND CIRCULATING CURRENT LOSSES OF THE AFPM GENERATOR AT RATED SPEED

	Disconnected coils (no circulating loss)			Parallel Connection	
	k_m	k_{eddy}	k_{eddy} (Analytical)	k_{eddy}	k_{circ}
Constants at 21.8ºC	0.171	0.589	0.583	0.589	1.980
Power Loss at 100rpm (W)	1.8	64.7	63.9	64.7	217.5

64.7 and 217.5 W, respectively. The eddy current loss using (5) shows good agreement compared to the measured value. Additionally, the mechanical loss estimated from Fig. 7 (1.8 W at rated speed) is very low due to the zero cogging torque in the air-cored machine.

3) Calculation of Rotor Losses: Rotor losses due to eddy currents are difficult to estimate analytically, and most of the literature on AFPM machines does not consider these losses in low-speed machines. The work in [25] suggests that rotor losses are relevant due to the fact that they act at a higher frequency compared to the fundamental frequency of the electric current. As the machine is connected to a resistive load bank and the EMF has negligible harmonics [23], the only relevant loss is induced by the first time harmonic component.

Finally, core resistance was measured using the direct-axis connection described in [28], using a magnetic analyzer (Wayne Kerr Electronics, model 3260B), that gives the equivalent impedance in the locked-rotor test. At ambient temperature, the rotor losses are about 16% of the total losses. Although this estimation is accurate in terms of aggregated losses, experimentally, it is very complex to segregate magnet from iron losses. A rather simple analytical approach is used here to segregate rotor losses.

4) Segregation of Rotor Losses: Eddy current loss per square area in magnets or iron can be modeled as

$$P_{\mathrm{eddy}} = \left(\hat{B}_0^2 v^2 \delta_i\right) / (4\rho_i) \tag{14}$$

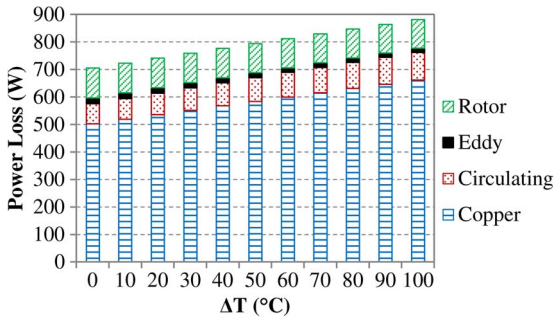

Fig. 8. Input losses for the CFD model at 100 r/min for a single stage. The copper loss (71%) is the major loss, whereas the eddy current loss in the windings represents only 3% of the total losses.

where $i = \{\mathrm{PM}, \mathrm{Fe}\}$. If the speed v of the flux density wave is the same for the entire rotor and assuming that the flux density from the armature reaction exponentially decays when reaching the back iron according to $\exp(-h_{\mathrm{PM}}/\delta_{\mathrm{PM}})$ [29], then it is possible to find that the magnet and iron losses have the ratio given by the following (see the Appendix for the derivation):

$$\frac{P_{\mathrm{eddy}_{\mathrm{Fe}}}}{P_{\mathrm{eddy}_{\mathrm{PM}}}} \approx \sqrt{\frac{\rho_{\mathrm{PM}}\mu_{\mathrm{PM}}}{\rho_{\mathrm{Fe}}\mu_{\mathrm{Fe}}}} e^{-2\frac{h_{\mathrm{PM}}}{\delta_{\mathrm{PM}}}}. \tag{15}$$

This assumption is questionable as (14) assumes that the skin depth of the magnets δ_{PM} is much smaller than the wavelength of the flux reaction; at 100 r/min, this is valid for the iron, but for the magnets, δ_{PM} is only 1.6 times smaller than the wavelength. Nevertheless, (15) multiplied by the total ratio of material volumes allows a reasonable distribution of the losses among magnets and iron. In this experiment, the estimated total loss ratio is 2.02 approximately.

5) Summary of Electrical Losses: Total load and no-load losses were measured at ambient temperature $(\Delta T_{\mathrm{coil}} = 0)$ using the methodology described in the previous sections. A breakdown of losses is depicted in Fig. 8. The extrapolation of losses according to temperature rise ΔT_{coil} is done by running a MATLAB script with equations from (5)–(10). Magnet and iron loss distribution is assumed to be approximately 2 : 1 according to (15) and their volume ratio, although Fig. 8 shows both losses aggregated. It can be seen that the only losses magnified by ΔT_{coil} are the copper $(3I_{\mathrm{rms}}R^2)$ and circulating current as the resistivity of the copper increases with temperature.

Finally, Fig. 9 illustrates the dynamic integration between the lookup table of input losses (summarized in Fig. 8) and the CFD. The CFD model updates the steady-state input loss in each iteration, until the temperature of the coil converges.

V. CFDs

Due to the improvement of numerical methods and computer power, modeling using CFD methods is now popular for electrical machine thermal analysis. The CFD software program STAR-CCM+ [30] was used in the present study.

A. Model Definition and Mesh

Since the AFPM machine is assembled from eight c-core rotor and stator modules arranged circumferentially to give one

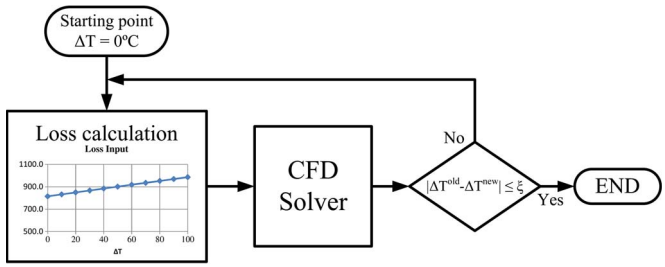

Fig. 9. Flow diagram of loss integration: CFD heat sources are mapped from the power losses as a function of ΔT_{coil}, allowing the simulation to upgrade the steady-state input loss in each iteration.

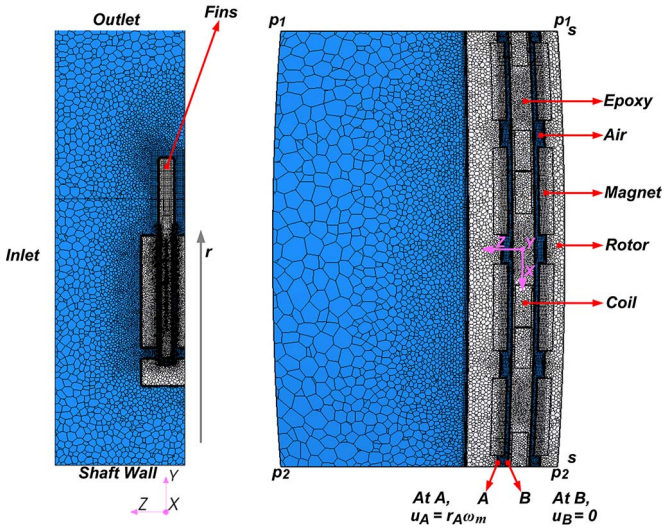

Fig. 10. Mesh of CFD domain. (Left) Side view and (right) internal view at radius $= 0.43$ m to indicate the machine components.

stage, only one-eighth (45°) segment was modeled in three dimensions for simulating flow and heat transfer. As shown in Fig. 10, symmetry and periodic planes of this segment are represented by $s-s$, p_1-p_1, and p_2-p_2, respectively. Alongside the fluid domain, the solid domain representing the rotor and stator was also included to calculate power dissipation via conduction. All material properties specified in the CFD model were the same as those of the prototype machine (i.e., magnets—NdFeB, coils—copper, fins—aluminum, rotor—cast iron, and stator core—epoxy resin). Conformal mesh interfaces between solid and fluid domains were created to maintain the continuity of heat flux and temperature.

Polyhedral and prism layer meshers were employed. Within the fluid regions, the minimum mesh size was set to be 0.0178 mm close to the walls, which corresponds to one-hundredth of the fluid boundary layer. However, the minimum mesh size for the solid regions was set to be 1 mm, which corresponds to one-twelfth of the coil thickness sufficient to calculate conductive heat transfer. The maximum mesh sizes of the fluid and solid regions were set 12 and 5 mm, respectively, to save the computational cost. The total number of computational cells of fluid is about 6 million, whereas for solid, it is about 2 million. The mesh in the fluid region is denser because of the advection term in the flow equations which is more difficult to resolve than pure conduction in the solid domain.

B. Turbulent Flow and Energy Modeling

As steady-state operation of the machine was investigated, steady-state models were chosen for the CFD simulation. The present study had made use of a rotating reference frame to simulate the relative motion of the rotor and stator for time-averaged steady-state solutions. As the rotor speed gives the peripheral Reynolds number of 1.4×10^5, a turbulence model was necessary. Two kinds of turbulent models, Realizable $k-\varepsilon$ and SST (Menter) $k-\omega$, were used to provide closure of the Reynolds-averaged Navier–Stokes equations in the present study, and these will be compared against each other. The effect of gravity is ignored. The air was assumed to be an ideal gas with constant viscosity, thermal conductivity, and specific heat. The governing equations of a steady fully turbulent flow can be represented in vector form as follows:

fluid continuity

$$\nabla \cdot \rho \overline{V} = 0 \tag{16}$$

fluid momentum

$$\overline{V} \cdot \nabla \rho \overline{V} = -\nabla \overline{p} + (\mu + \mu_t) \nabla^2 \overline{V} \tag{17}$$

fluid energy

$$c_p \overline{V} \cdot \nabla \rho \overline{T} = (k_{\mathrm{air}} + k_t) \nabla^2 \overline{T} \tag{18}$$

solid energy

$$k_{\mathrm{sol}} \nabla^2 T + S_T = 0. \tag{19}$$

The enhanced diffusion due to the turbulent eddies is taken into account by the turbulent viscosity μ_t and turbulent conductivity k_t. They are related through the turbulent Prandtl number $\mathrm{Pr}_t = 0.7$. Turbulence kinetic energy is caused by velocity fluctuations and is dissipated by viscosity. The transport equations of turbulent kinetic energy k and dissipation rate ε for the Realizable $k-\varepsilon$ model are

$$\overline{V} \cdot \nabla \rho k = \nabla \cdot \left[\left(\mu + \frac{\mu_t}{\sigma_k} \right) \nabla k \right] + P_k - \rho \varepsilon \tag{20}$$

$$\overline{V} \cdot \nabla \rho \varepsilon = \nabla \cdot \left[\left(\mu + \frac{\mu_t}{\sigma_\varepsilon} \right) \nabla \varepsilon \right] + C_1 \rho \sqrt{2 S_{ij} S_{ij}} \varepsilon - C_2 \rho \varepsilon^2 \Big/ \left[k + \left(\frac{\mu_t \varepsilon}{\rho} \right)^{1/2} \right]. \tag{21}$$

The turbulent viscosity μ_t for the Realizable $k-\varepsilon$ model is computed as

$$\mu_t = \rho C_\mu \frac{k^2}{\varepsilon} \tag{22}$$

$$P_k = 2 \mu_t S_{ij} \cdot S_{ij} - \frac{2}{3} \rho k \nabla \cdot V - \frac{2}{3} \mu_t (\nabla \cdot V)^2. \tag{23}$$

S_{ij} is the strain rate tensor. The turbulence model coefficients σ_k, σ_ε, and C_2 and the auxiliary relations of C_1 and C_μ are described in [30].

The transport equations of turbulent kinetic energy k and specific dissipation rate ω for the SST $k-\omega$ model are

$$\overline{V}\cdot\nabla\rho k=\nabla\cdot[(\mu+\sigma_k\mu_t)\nabla k]+P_k-\rho\beta^*k\omega \quad (24)$$

$$\overline{V}\cdot\nabla\rho\omega=\nabla\cdot[(\mu+\sigma_\omega\mu_t)\nabla\omega]+\rho\gamma G_\omega-\rho\beta\omega^2+2(1-F_1)\frac{\rho\sigma_{\omega2}}{\omega}\nabla k\cdot\nabla\omega. \quad (25)$$

For the SST $k-\omega$ model, the Durbin realizability constraint ($C_T=0.6$) was applied and imposed on the turbulent viscosity formula (26) to overcome an unexpectedly large growth of k in stagnation point flows. Hence, the turbulent viscosity μ_t is computed as

$$\mu_t=\rho k\min\left[\frac{1}{\max(\omega,F_2\sqrt{2S_{ij}S_{ij}}/a_1)},\frac{C_T}{\sqrt{6S_{ij}S_{ij}}}\right] \quad (26)$$

$$G_\omega=2S_{ij}\cdot S_{ij}-\frac{2}{3}\omega\nabla\cdot V-\frac{2}{3}(\nabla\cdot V)^2. \quad (27)$$

The turbulence model coefficients and auxiliary relations of a_1, β^*, β, F_1, F_2, γ, σ_k, σ_ω, and $\sigma_{\omega2}$ are described in [30].

C. Boundary Conditions

The governing equations are subjected to the following boundary conditions.

At the inlet, the total gauge pressure $p_{\rm tot}=0$ Pa and the inlet temperature $=29$ °C (ambient). At the outlet, the static pressure $p=0$ Pa and the opening entrainment temperature $=29$ °C. At both the inlet and outlet, the turbulent kinetic energy and dissipation rate were set at default to be 0.001 J $\cdot$ kg^{-1} and 0.1 J $\cdot$ kg^{-1} $\cdot$ s^{-1}, respectively, whereas the specific dissipation rate was set to be 1×10^{-4} s^{-1}.

Both rotor and stator surfaces are smooth and have no slip. The local speed of the rotor surface is equal to $r\omega_m$. At the wall (solid–fluid interface), the air temperature is equal to T_w. Hence,

$$(k_{\rm air}+k_t)\nabla^2T=k_{\rm sol}\nabla^2T. \quad (28)$$

The power loss described in Section IV is coupled with the CFD model as internal heat generation. The heat generation per unit volume S_T varies according to the temperature rise of the solid component from ambient temperature

$$S_T=f(\Delta T_{\rm coil}). \quad (29)$$

D. Wall Treatment

As the turbulence models are valid only outside the viscous-affected region of the boundary layer, a wall treatment model was adopted to specify profiles of the mean flow quantities in the wall boundary layers. The flow velocity and wall distance in the near-wall region are expressed in dimensionless form as

$$u^+=\frac{u}{\sqrt{\tau_w/\rho}} \quad (30)$$

$$y^+=\frac{y\rho\sqrt{\tau_w/\rho}}{\mu}. \quad (31)$$

τ_w is the wall shear stress, u is the mean velocity parallel to the wall, and y is the normal distance from the wall. The near-wall turbulent boundary layers can be divided into three layers. In the innermost viscous sublayer ($y^+<5$), the velocity profile is

$$u^+=y^+. \quad (32)$$

In the outer turbulent layer ($y^+>30$), u^+ varies logarithmically with y^+ as follows ($E=9$ for a smooth wall):

$$u^+=\frac{1}{0.42}\ln(Ey^+). \quad (33)$$

Between these two layers (i.e., a buffer layer), u^+ is obtained using Reichardt's law, blending the viscous sublayer and logarithmic velocity profiles. With the intention of resolving the viscous sublayer, a high boundary layer mesh resolution was created with the wall cell $y^+\leq1$. Due to the low rotor speed, the *all y^+ wall treatment* approach was used to compute the wall shear stress, turbulent production, and turbulent dissipation.

E. Solution Strategy

The governing equations were numerically discretized using a finite-volume method to a system of linear algebraic equations. These were solved simultaneously based on the conservation of mass, momentum, energy, and turbulence parameters using the second-order upwind discretization scheme. However, only the conservation equation for energy was solved for the solid regions.

In the CFD models, each stator coil was simplified by a bulk copper region. As the materials of insulation and impregnation of windings were not physically modeled, the composite thermal resistance per unit area is computed as

$$R_{\rm th}=\sum_{i=1}^{n}\left(\frac{l_i}{k_i}\right)+\sum_{j=1}^{n}\left(\frac{l_j}{k_j}\right). \quad (34)$$

l_i and l_j are the thicknesses of insulation and impregnation, respectively, k_i and k_j are the thermal conductivities of insulation and impregnation, respectively, and n is the number of winding layers. The conductive resistance was applied as the thermal contact resistance of the interfaces between copper and epoxy regions.

VI. Comparison and Discussion

The simulated results agree reasonably well with the experimental results in Table II. This comparison demonstrates that the CFD models are capable of predicting the impact of inlet configuration on the machine cooling. The discrepancy between experimental and CFD results arises from the fact that the actual power losses are not uniformly distributed throughout the volumes of the corresponding machine parts as modeled in CFD and some limitations of the chosen turbulence models.

TABLE II
MEASURED AND SIMULATED TEMPERATURE RISES (IN DEGREES CELSIUS) AFTER STEADY STATE ($T_{\text{ambient}} = 29\,^{\circ}\text{C}$ AND Speed = 100 r/min)

CASE 1: VENTILATION WITH RADIAL AND AXIAL HOLES

Temperature Rise	Experiment	CFD (Realizable k-ε)		CFD (SST k-ω)	
Thermocouple A	52.6	47.3	-10.08%	54.1	2.85%
Thermocouple B	58.2	49.3	-15.29%	57.0	-2.06%
Thermocouple C	35.6	36.5	2.53%	42.3	18.82%
Rotor $_{\text{mean}}$	-	18.9	-	22.3	-
Magnet $_{\text{mean}}$	-	22.2	-	25.9	-
Coil $_{\text{mean}}$	-	50.3	-	57.5	-

Case 2: Ventilation With Radial Holes Only

Temperature Rise	Experiment	CFD (Realizable k-ε)		CFD (SST k-ω)	
Thermocouple A	56.4	53.3	-5.50%	58.7	4.08%
Thermocouple B	62.4	55.9	-10.42%	63.7	2.08%
Thermocouple C	40.3	30.2	-2.73%	47.5	17.87%
Rotor $_{\text{mean}}$	-	23.7	-	27.5	-
Magnet $_{\text{mean}}$	-	27.4	-	31.4	-
Coil $_{\text{mean}}$	-	56.9	-	64.2	-

Case 3: Ventilation With Axial Holes Only

Temperature Rise	Experiment	CFD (Realizable k-ε)		CFD (SST k-ω)	
Thermocouple A	59.5	63.4	6.55%	72.0	21.01%
Thermocouple B	67.0	66.2	-1.19%	77.1	15.07%
Thermocouple C	44.1	46.0	4.31%	57.3	29.93%
Rotor $_{\text{mean}}$	-	31.5	-	38.0	-
Magnet $_{\text{mean}}$	-	36.6	-	43.4	-
Coil $_{\text{mean}}$	-	67.3	-	77.5	-

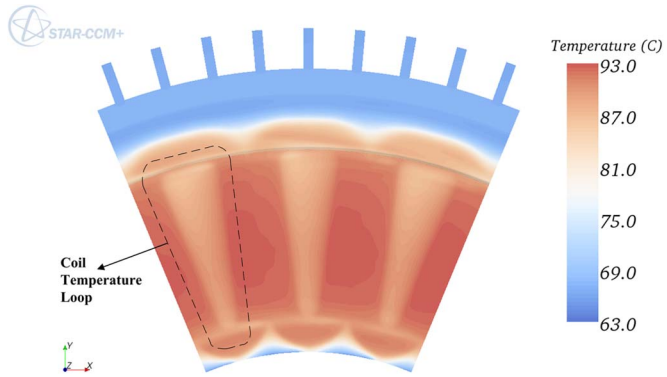

Fig. 11. Temperature contour of the stator surface for Case 2; CFD (SST $k-\omega$).

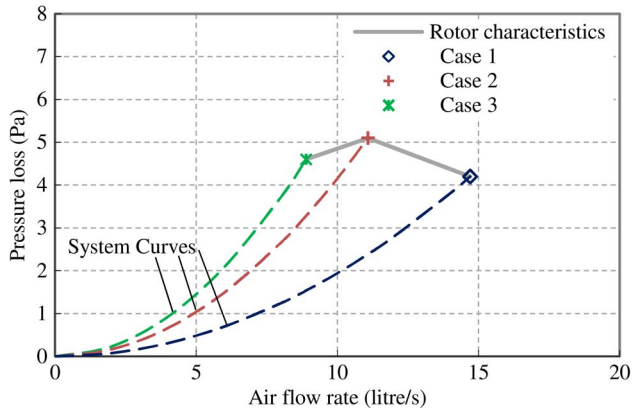

Fig. 12. System flow resistance for different inlet configurations; CFD (Realizable $k-\varepsilon$). Rotor speed = 100 r/min. The dashed lines representing system curves were obtained by extrapolating from the CFD results using (4).

As the stator coils generate the main heat, higher temperatures can be seen around the coils. This forms a coil temperature "loop" as illustrated in Fig. 11. The experimental results indicate that the maximum temperature rise (thermocouple B) of Case 3 is about 15% higher than that of Case 1. This demonstrates that the inlet configuration can substantially affect machine cooling. Although the AFPM prototype performance in the present study is well within the temperature limits, cooling becomes a very important issue for machines with high power density such as large-scale wind turbine generators. Therefore, AFPM machine cooling needs efficient ventilation to avoid overheating.

Windage torque of the AFPM generator has a shear and pressure component. Shear torque is used to overcome the air friction for rotating parts while pressure torque is converted into rotor pumping pressure. From CFD modeling, the windage losses of the entire AFPM machine for Case 1, Case 2, and Case 3 are 1.63, 1.47, and 1.34 W, respectively (values of the nondrive end stage multiplied by three), where windage losses are part of the mechanical losses but negligible compared to the major loss components described in Section IV. Fig. 12 shows the variation of the system pressure loss and total air flow rate through the nondrive end stage for different inlet configurations.

The inlet flow rate of Case 2 is higher than that of Case 3 because the flow through the axial holes experiences an additional bending loss. Case 1 shows the highest inlet flow rate because the sum of its inlet areas is two times bigger, and hence, higher air flow rate results in greater stator convective heat transfer. To obtain a higher flow rate, an external fan can be connected to the system. However, the corresponding system flow resistance will remain the same. Since the windage loss is negligible at the running speed, it does not result in a significant efficiency decease. In contrast, a lower temperature rise may reduce the electromagnetic losses for those losses that are temperature dependent.

As shown in Fig. 13, the mean stator convective heat transfer $\overline{\text{Nu}}$ at the radial position is calculated for $0.65 \leq r/R \leq 1$ (the area where the stator faces the magnet protrusions on the rotor) as follows:

$$\overline{h} = q''/(T_w - T_{\text{ref}}) \tag{35}$$

$$\overline{\text{Nu}} = \overline{h}r/k_{\text{air}}. \tag{36}$$

The predicted CFD results were compared with Howey's correlation which is valid at gap ratio $G = 0.0106$. Since the empirical correlation is developed based on the convention of using ambient fluid temperature as the reference temperature, this convention is also followed. In fact, the air entering the machine tends to circulate in the rotor-stator gap in the tangential direction while it is being pumped radially outward. The air temperature increases along the rotor-stator gap. Hence,

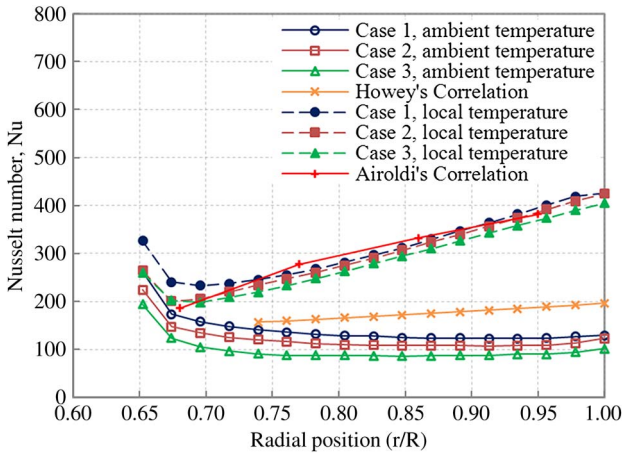

Fig. 13. Comparison of stator convective heat transfer between CFD (Realizable $k-\varepsilon$) and heat transfer correlations.

using the ambient fluid temperature tends to give conservative estimation of stator convective heat transfer. Based on heat transfer and fluid dynamic practice, $T_{\rm ref}$ should refer to the local fluid bulk temperature at the radius where the calculation for convective heat transfer coefficient is being made. The Nusselt numbers based on the local air temperature are also shown in Fig. 13. They were compared with the more comprehensive Airoldi correlation which is also based on the local air temperature. It can be seen that they are considerably higher than the values calculated based on the ambient temperature, particularly at the outer radii. Overall, the simulated results agree reasonably well with the values obtained from the stator heat transfer correlations. The predicted Nusselt numbers based on ambient temperature are lower than the values obtained from Howey's correlation because the AFPM machine of the present study has smaller gap ratio.

VII. Conclusion

The detailed distribution of power losses of an AFPM generator has been presented in this paper. These losses are converted into heat, causing the temperature rise of machine parts, and this has been modeled through CFD and validated in an actual AFPM direct-drive generator with surface-mounted magnets. The present study has demonstrated the impact of inlet configuration on generator cooling for the rated speed. The more efficient the ventilation system can be made, the greater the performance that can be achieved from a given electrical machine while still maintaining the temperature within proper limits. From a design point of view, electrical machines should not have a degree of enclosure more than absolutely necessary.

Appendix

For estimating the ratio between iron and magnet losses, the next assumptions are considered.

1) At the rated speed, the skin depth for magnets and iron is much smaller than the wavelength of the flux reaction that causes eddy current losses.
2) Phase currents are sinusoidal as the machine is connected to a resistive load bank. Therefore, the main loss is produced by the fundamental time harmonic.
3) The winding arrangement for this machine (known as the nonoverlapping concentrated winding) produces a fundamental space harmonic which contributes to most of eddy current losses. The second space harmonic rotates synchronously to the rotor [31].

Then, eddy current losses per square area in magnets and iron can be modeled by

$$P_{\mathrm{eddy}_{\mathrm{PM}}} = (\hat{B}_{0\mathrm{PM}}^2 v^2 \delta_{\mathrm{PM}})/(4\rho_{\mathrm{PM}}) \tag{37}$$

$$P_{\mathrm{eddy}_{\mathrm{Fe}}} = (\hat{B}_{0\mathrm{Fe}}^2 v^2 \delta_{\mathrm{Fe}})/(4\rho_{\mathrm{Fe}}) \tag{38}$$

where the skin depth is defined as

$$\delta_i = \sqrt{(\rho_i/(\mu_0 \mu_r \pi f))}. \tag{39}$$

$\hat{B}_0^2$ is the peak value of the flux caused by the fundamental space harmonic. Due to the exponential decay of the flux reaction, crossing the magnets, the peak flux density in the iron is given by

$$B_{0\mathrm{Fe}} = B_{0\mathrm{PM}} \cdot e^{-h_{\mathrm{PM}}/\delta_{\mathrm{PM}}}. \tag{40}$$

By simple algebra, it is possible to derive the ratio of losses (15) between the two materials.

Acknowledgment

This work has made use of the resources provided by the Edinburgh Compute and Data Facility (ECDF) (http://www.ecdf.ed.ac.uk/). The ECDF is partially supported by the E-Science Data Information and Knowledge Transformation initiative (http://www.edikt.org.uk). The authors would like to thank P. Valluri and O. Keysan, who have provided help and advice to this work.

References

[1] J. Hey and D. Howey, "Transient thermal modeling of an axial flux permanent magnet (AFPM) machine using a hybrid thermal model," *Int. J. Mech. Mater. Eng.*, vol. 1, no. 3, pp. 150–159, 2010.
[2] A. Di Gerlando, G. Foglia, M. F. Iacchetti, and R. Perini, "Axial flux PM machines with concentrated armature windings: Design analysis and test validation of wind energy generators," *IEEE Trans. Ind. Electron.*, vol. 58, no. 9, pp. 3795–3805, Sep. 2011.
[3] M. A. Mueller and A. S. McDonald, "A lightweight low-speed permanent magnet electrical generator for direct-drive wind turbines," *Wind Energy*, vol. 12, no. 8, pp. 768–780, Nov. 2009.
[4] N. Hodgins, O. Keysan, A. S. McDonald, and M. A. Mueller, "Design and testing of a linear generator for wave–energy applications," *IEEE Trans. Ind. Electron.*, vol. 59, no. 5, pp. 2094–2103, May 2012.
[5] X. Sun and M. Cheng, "Thermal analysis and cooling system design of dual mechanical port machine for wind power application," *IEEE Trans. Ind. Electron.*, vol. 60, no. 5, pp. 1724–1733, May 2013.
[6] F. Marignetti, V. D. Colli, and Y. Coia, "Design of axial flux PM synchronous machines through 3-D coupled electromagnetic thermal and fluid-dynamical finite-element analysis," *IEEE Trans. Ind. Electron.*, vol. 55, no. 10, pp. 3591–3601, Oct. 2008.

[7] A. Boglietti, S. Member, A. Cavagnino, D. Staton, M. Shanel, M. Mueller, and C. Mejuto, "Evolution and modern approaches for thermal analysis of electrical machines," *IEEE Trans. Ind. Electron.*, vol. 56, no. 3, pp. 871–882, Mar. 2009.
[8] D. A. Staton and A. Cavagnino, "Convection heat transfer and flow calculations suitable for electric machines thermal models," *IEEE Trans. Ind. Electron.*, vol. 55, no. 10, pp. 3509–3516, Oct. 2008.
[9] D. Staton, A. Boglietti, and A. Cavagnino, "Solving the more difficult aspects of electric motor thermal analysis in small and medium size industrial induction motors," *IEEE Trans. Energy Convers.*, vol. 20, no. 3, pp. 620–628, Sep. 2005.
[10] P. R. N. Childs, *Rotating Flow*, 1st ed. Oxford, U.K.: Butterworth-Heinemann, 2011, pp. 81–126.
[11] G. Batchelor, "Note on a class of solutions of the Navier–Stokes equations representing steady rotationally-symmetric flow," *Quart. J. Mech. Appl. Math.*, vol. 4, no. 1, pp. 29–41, 1951.
[12] K. Stewartson, "On the flow between two rotating coaxial discs," *Math. Proc. Cambridge Philosph. Soc.*, vol. 49, no. 2, pp. 333–341, 1953.
[13] J. Owen and R. Rogers, "Flow and heat transfer in rotating-disc systems," in *Rotor–Stator Systems*, 1st ed. Taunton, U.K.: Research Studies Press, 1989.
[14] D. A. Howey, P. R. N. Childs, and A. S. Holmes, "Air-gap convection in rotating electrical machines," *IEEE Trans. Ind. Electron.*, vol. 59, no. 3, pp. 1367–1375, Mar. 2012.
[15] R. Boutarfa and S. Harmand, "Local convective heat transfer for laminar and turbulent flow in a rotor–stator system," *Exp. Fluids*, vol. 38, no. 2, pp. 209–221, Feb. 2005.
[16] D. A. Howey, A. S. Holmes, and K. R. Pullen, "Measurement and CFD prediction of heat transfer in air-cooled disc-type electrical machines," *IEEE Trans. Ind. Appl.*, vol. 47, no. 4, pp. 1716–1723, Jul./Aug. 2011.
[17] J. Daily and R. Nece, "Chamber dimension effects on induced flow and frictional resistance of enclosed rotating dicks," *Trans. ASME, J. Basic Eng.*, vol. 82, no. 1, pp. 217–232, 1960.
[18] Y. C. Chong, J. Chick, M. A. Mueller, D. A. Staton, and A. S. McDonald, "Thermal modelling of a low speed air-cooled axial flux permanent magnet generator," in *Proc. 6th IET Int. Conf. Power Electron. Mach. Drives*, Bristol, U.K., 2012, pp. 1–7.
[19] S. T. Scowby, R. T. Dobson, and M. J. Kamper, "Thermal modelling of an axial flux permanent magnet machine," *Appl. Thermal Eng.*, vol. 24, no. 2/3, pp. 193–207, Feb. 2004.
[20] G. Airoldi, "Numerical investigations of air flow and heat transfer in axial flux permanent magnet machines," Ph.D. dissertation, Durham Univ., Durham, U.K., 2010.
[21] R. J. Wang, M. J. Kamper, and R. T. Dobson, "Development of a thermofluid model for axial field permanent-magnet machines," *IEEE Trans. Energy Convers.*, vol. 20, no. 1, pp. 80–87, Mar. 2005.
[22] J. F. Douglas, J. M. Gasiorek, and J. A. Swaffield, *Fluid Mechanics*, 3rd ed. Singapore: Longman, 1995, pp. 145–189.
[23] A. S. McDonald, M. Benatmane, and M. A. Mueller, "A multi-stage axial flux permanent magnet machine for direct drive wind turbines," in *Proc. 1st IET Conf. Renewable Power Generation*, Edinburgh, U.K., 2011, pp. 1–6.
[24] R. D. Stefano and F. Marignetti, "Electromagnetic analysis of axial-flux permanent magnet synchronous machines with fractional windings with experimental validation," *IEEE Trans. Ind. Electron.*, vol. 59, no. 6, pp. 2573–2582, Jun. 2012.
[25] E. Echenique, M. A. Mueller, T. Bertenyi, and T. Young, "Realistic loss modelling and minimisation in an air-cored permanent magnet generator for wind energy applications," in *Proc. 6th IET Int. Conf. Power Electron. Mach. Drives*, Bristol, U.K., 2012, pp. 1–6.
[26] G. W. Carter, *The Electromagnetic Field in Its Engineering Aspect*, 2nd ed. London, U.K.: Longman, 1967.
[27] R. Wang and M. J. Kamper, "Evaluation of eddy current losses in axial flux permanent magnet (AFPM) machine with an ironless stator," in *Conf. Rec. IEEE 37th IAS Annu. Meeting*, 2002, vol. 2, pp. 1289–1294.
[28] P. H. Mellor, "Estimation of parameters and performance of rare-earth permanent-magnet motors avoiding measurement of load angle," in *Proc. Inst. Elect. Eng.—B Elect. Power Appl.*, Nov. 1991, vol. 138, no. 6, pp. 322–330.
[29] R. Stoll, *The Analysis of Eddy Currents*. Oxford, U.K.: Clarendon, 1974.
[30] *User Guide STAR-CCM + Version 6.04.014*, CD-adapco, Melville, NY, USA, 2011.
[31] P. J. Randewijk and M. J. Kamper, "Analytical analysis of a radial flux air-cored permanent magnet machine with a double-sided rotor and non-overlapping double-layer windings," in *Proc. 20th Int. Conf. Elect. Mach.*, Marseille, France, 2012, pp. 1178–1184.

Yew Chuan Chong received the B.Eng.Hons. and M.Eng. degrees in mechanical engineering from Staffordshire University, Stafford, U.K., in 2006 and 2007, respectively. He is currently working toward the Ph.D. degree at the Institute for Energy Systems, The University of Edinburgh, Edinburgh, U.K., under the Energy Technology Partnership's Energy Industrial Doctorate Program, collaborating with Motor Design Ltd., developing analytical design tool to model the air flow in electrical machines.

His current research interests include the thermal analysis of electrical machines, mechanical design, and thermofluids.

Estanislao J. P. Echenique Subiabre was born in Rancagua, Chile. He received the B.S. and M.Sc.-(Hons.) degrees in electrical engineering from the Pontificia Universidad Católica de Chile, Santiago, Chile, in 2008. He is currently working toward the Ph.D. degree at the Institute for Energy Systems, The University of Edinburgh, Edinburgh, U.K.

He has worked as a Consulting Engineer with System Engineering and Designs and also on research projects in power electronics, electric vehicles with photovoltaic cells, and antiseismic instrumentation. His main interests include power electronics, machine control for renewable energy, and artificial intelligence applied to machine control.

Mr. Echenique Subiabre was the recipient of the "Ramón Salas Edwards" Award in 2009 for the paper "Sensorless Control for a Switched Reluctance Wind Generator, Based on Current Slopes and Neural Networks" published in the IEEE TRANSACTIONS ON INDUSTRIAL ELECTRONICS.

Markus A. Mueller (M'05) received the B.Sc.-(Eng.) degree in electrical engineering from Imperial College, London, U.K., in 1988 and the Ph.D. degree from the University of Cambridge, Cambridge, U.K., for his work on modeling induction motors.

He subsequently worked as a Postdoctoral Fellow with the University of Cambridge in collaboration with Brook Crompton Motors. After two years with SR Drives Ltd. as a Senior Development Engineer, in 1997, he was appointed as Lecturer at Durham University, Durham, U.K. Since January 2004, he has been with The University of Edinburgh, Edinburgh, U.K., where he holds a Personal Chair in Electrical Machines. In 2009, he founded NGenTec Ltd. to scale up and commercialize the C-GEN technology for the offshore wind sector. He is the author of 100 papers and is the inventor of C-GEN, for which two patents have been filed. His main research interests include the design of electrical machines for renewable energy converters.

Prof. Mueller was a recipient of the Donald Julius Groen Prize from the Institution of Mechanical Engineers for his work on direct-drive linear generators for wave–energy converter in 2006.

John Chick received the B.Eng. degree in mechanical engineering and the Ph.D. degree from The University of Nottingham, Nottingham, U.K., in 1994 and 1998, respectively. The subject of his Ph.D. thesis was heat transfer modeling in internal combustion engines and was carried out in close collaboration with the U.K. Research and Development Centre, Ford, Dunton, U.K.

Since 1999, he has been a Lecturer with the School of Engineering, The University of Edinburgh, Edinburgh, U.K. His active research interests are in heat transfer, wind energy, and acoustics.

David A. Staton received the Ph.D. degree in computer-aided design of electrical machines from The University of Sheffield, Sheffield, U.K., in 1988.

He worked on motor design and, particularly, the development of motor design software at Thorn EMI, the SPEED Laboratory, University of Glasgow, Glasgow, U.K., and Control Techniques, U.K. In 1999, he set up Motor Design Ltd., Ellesmere, U.K., to develop thermal analysis software for electrical machines. He has published over 100 papers in conferences and peer-reviewed journals.

Alasdair S. McDonald received the B.S. degree (first-class honors) in electrical and mechanical engineering from Durham University, Durham, U.K., in 2004 and the Ph.D. degree from The University of Edinburgh, Edinburgh, U.K., in 2008.

During his doctoral years, he developed analytical design tools for the structure of direct-drive generators. In 2012, he was appointed as Lecturer in the Department of Electronic and Electrical Engineering, University of Strathclyde, Glasgow, U.K., where he specializes in wind turbine drivetrain design and modeling.